RESEARCH ARTICLE

ADVANCED MATERIALS
www.advmat.de

Versatile Room-Temperature Phosphorescence Silk Fibroin Platforms for Sustainable and Biocompatible Multifunctional Interfaces

Tao Wang, Ying-Hao Fu, Jing Wang, Gang Li, Jing Sun, Qi Liu, Yan-Tong Zhao, Zi-Chen Zhang, Zi-Ting Wang, Shu-Jie Wang, Zhao-Zhu Zheng, Yu Wang, and Yan-Qing Lu**

The development of sustainably sourced, biocompatible room-temperature phosphorescence (RTP) materials with rich formats, multimodal tunability, and multifunctional capabilities presents a transformative opportunity for sustainable technologies and biomedical interfaces, yet it remains a significant challenge. Here, RTP silk fibroin systems that feature improved processability, responsiveness, and functionality by multivalently anchoring phosphors to a versatile protein matrix are reported. The RTP silk fibroin can be processed into various fully biodegradable platforms, exhibiting strong RTP emission with a lifetime of up to 233 ms driven by multiple robust phosphor–fibroin interactions. The resulting platforms exhibit multi-responsiveness to UV light, vapor, and temperature, along with diversified functionalities that include recyclability, weldability, morphability, and adhesion. Moreover, their adaptability with diverse micro/nano-processing techniques enables complex RTP patterning and multidimensional information integration. Finally, it is demonstrated that these convergent advantages endow the platforms with multifunctionality and multi-interface compatibility, enabling applications such as smart labels for electronic devices, conformal networks for pharmaceuticals, and scalable textiles for face masks.

1. Introduction

Long-lived organic room-temperature phosphorescence (RTP) is emerging as an attractive photoluminescence technology in the fields of photonics and electronics, owing to its large Stokes shift, high signal-to-noise ratio, tunable optical signatures, and low cost.[1,2] These distinct attributes lead to the remarkable success of long-lived organic RTP materials in widespread application areas, from information encryption,[3] anti-counterfeiting,[4] and sensing[5] to afterglow displays,[6] thermal management,[7] and bio-imaging.[8] In recent decades, various productive strategies have been developed for achieving highly efficient and long-lived organic RTP, including crystal engineering,[1] self-assembly,[9] encapsulation,[10,11] or polymerization.[4,12] These approaches effectively suppress non-radiative transitions of excitons from the excited triplet state to the ground state by constructing a rigid molecular environment that controls the motion of phosphors and isolates oxygen and water molecules. A diverse set of long-lived organic RTP systems has been progressively developed based on these strategies. Among these systems, polymer-based long-lived RTP materials stand out due to their tunable mechanical properties, design flexibility, and ease of processability and formability.[13,14] In particular, the low-cost, large-scale, and flexible production guarantees the widespread adoption and commercialization of polymer-based RTP materials.

The general approach to creating RTP polymeric systems involves physically and/or chemically incorporating phosphors into polymer matrices. The physical method relies on non-covalent interactions, such as hydrogen bonding networks, electrostatic interactions, or van der Waals forces, between phosphors and polymer chains to activate RTP generation.[12,15,16] while the chemical method involves directly attaching phosphors to the polymer chain via strong, stable covalent bonds.[17,18] Following these strategies, polymer-based RTP materials have seen remarkable advancements in molecular and microstructural design,[17,19,20] mechanism exploration,[21] lifetime improvement,[6] dynamic modulation,[22] multicolor afterglow,[5,16] chiral luminescence,[23,24] robust mechanical performance,[12] and resistance to high temperatures,[25]

T. Wang, Y.-H. Fu, J. Wang, G. Li, Z.-C. Zhang, Z.-T. Wang, S.-J. Wang, Y. Wang, Y.-Q. Lu
National Laboratory of Solid State Microstructures
Key Laboratory of Intelligent Optical Sensing and Manipulation
College of Engineering and Applied Sciences and Collaborative Innovation Center of Advanced Microstructures
Nanjing University
Nanjing 210023, China
E-mail: yuwang87@nju.edu.cn; yqlu@nju.edu.cn

J. Sun, Q. Liu, Y.-T. Zhao, Z.-Z. Zheng
National Engineering Laboratory for Modern Silk
Soochow University
Suzhou 215123, China

The ORCID identification number(s) for the author(s) of this article can be found under https://doi.org/10.1002/adma.202512659

DOI: 10.1002/adma.202512659

among others. Recent years have witnessed growing interest in replacing petroleum-derived polymers with natural-resource-based alternatives for creating RTP materials.[26–31] This shift is driven by the fact that biomass materials not only align with sustainable development and support the value-added recycling of natural waste resources but also offer bio-functional properties such as biocompatibility and biodegradability, which enhance their potential for environmentally friendly and biocompatible technologies and applications. However, current biomass-derived RTP platforms (e.g., those based on cellulose, chitosan, or sodium alginate) remain limited by inflexible material forms, restricted responsiveness, and the difficulties in attaining complex functional integration, hindering their adaptability for multifunctional and multi-interface applications. Consequently, a novel RTP platform that merges sustainable sourcing and inherent biocompatibility with manifold material configurations, scalable processing, enhanced responsiveness, and multifunctionality is essential to meet the varied requirements of multiple applications.

Silk fibroin (SF) derived from native *Bombyx mori* silkworm fibers has shown significant potential as a sustainable biopolymer[32,33] for applications ranging from biomedicine,[34] optics,[35,36] and electronics,[34,37] to smart machines.[38] Rich in a diverse array of amino acids and exhibiting abundant surface chemistry, SF can be chemically modified to impart new optical, mechanical, and biological functionalities.[39] SF is particularly appealing for optical platforms due to its exceptional and versatile material characteristics, which, in addition to its sustainability and biodegradability, include tailorable structures, outstanding mechanical properties, diverse material forms, water-based processability at ambient temperature and pressure, and multi-scale manufacturing capabilities.[40] Of particular importance, the intrinsic structural “variability” under external stimuli endows the SF material with exceptional dynamic tunability, offering the possibility to create reconfigurable, tunable, and reprogrammable optical devices.[41] Furthermore, the ability to incorporate biotic/abiotic components into an aqueous SF solution adds new predesigned functions to the silk matrix, opening opportunities for developing multifunctional devices. The confluence of these distinctive material properties positions SF as a promising platform for creating sustainable and versatile RTP materials that address the challenges faced by existing polymer-based RTP systems. Although several silk-based RTP materials have been reported,[42–44] these systems suffer from intrinsic limitations in phosphorescent performance and have yet to fully harness the versatile material attributes of SF, thereby significantly constraining their applicability across diverse domains.

In this work, by incorporating phosphors with boronic acid groups into SF molecular chains through a rapid dehydration condensation reaction, we successfully created long-lived RTP silk fibroin (RTP-SF) materials that exhibit improved processability, tunability, functionality, and utility, while maintaining inherent sustainability and biocompatibility. We propose that the combined effects of B—O covalent bonding, hydrogen bonding, electrostatic interactions, and Van der Waals forces between arylboronic acid molecules and SF chains restrict phosphor motion and non-radiative transitions, thus promoting RTP emission. We illustrate SF’s capability to enable phosphorescent platforms in various forms with enhanced functionality. We demonstrate that RTP-SF’s multi-stimuli responsiveness facilitates the creation of reconfigurable and tunable phosphorescent platforms. We successfully developed complex, multicolored, and high-resolution RTP patterns using multimodal micro/nanopatterning techniques and established multidimensional optical systems by integrating hierarchical manufacturing approaches. Finally, we showcase the platform’s multifunctional capability and multi-interface compatibility through three demonstrators: a smart label for electronic devices, a conformal network for medicines, and a scalable textile for face masks.

2. Results

2.1. RTP-SF with Superior Comprehensive Material Attributes

SF features a complex primary structure consisting of a heavy chain (H-chain) and a light chain (L-chain) linked by a disulfide bond, along with a glycoprotein called P25, in a molar ratio of 6:6:1.[45] An SF H-chain (**Figure 1A**) comprises 12 highly repetitive domains flanked by 11 nonrepetitive motifs.[46] Both types of domains are rich in chemically active amino acids with functional groups (Figure 1B), such as serine and tyrosine with hydroxyl (—OH) side chains, and glutamic acid and aspartic acid with carboxyl side (—COOH) chains, which can serve as active sites for various chemical customization.[39] Therefore, phosphors, such as aromatic compounds, can be effectively grafted onto SF using specific chemical reactions. Previous studies have shown that arylboronic acids and arylboronic esters exhibit exceptional phosphorescent properties in rigid polymer environments, and the presence of boronic acid units facilitates the formation of covalent linkages with polymer matrices containing hydroxyl groups,[16,28] through click or dehydration condensation reaction. Taking inspiration from this, arylboronic acids with various π conjugations, such as 3-biphenylboronic acid (Bp-B), 1-naphthylboronic acid (Nap-B), and 1-pyrenylboronic acid (Py-B), were selected for anchoring to SF chains through a simple dehydration condensation reaction facilitated by the addition of ammonia water (Figure 1C). The resulting RTP-SFs were designated as SF-Bp-B, SF-Nap-B, and SF-Py-B, respectively. These phosphors can be securely anchored within the rigid SF matrix, effectively restricting molecular thermal motion and facilitating RTP emission with long lifetimes. On the one hand, this anchoring effect arises from the strong B—O covalent bonding between hydroxyl and carboxyl groups SF molecular chains and hydroxyl groups of arylboronic acids (Figure 1C). On the other hand, the abundant hydrogen-bonding interactions formed between arylboronic acids and SF chains, as well as within the SF chains themselves, further confine the phosphors. In addition to molecular-scale anchoring, the secondary and condensed state structures[47] formed at the larger scales of the SF molecular chains further enhance these interactions, thereby improving the RTP performance.

Beyond offering a favorable rigid environment for stabilizing phosphors, the employment of SF imparts the final RTP materials with a multitude of distinctive attributes, including varied material formats, multi-stimulus responsiveness, multilevel processability, and functional diversity (Figure 1D). Starting from the aqueous RTP-SF solution, RTP materials with multidimensional structures can be obtained by combining SF self-assembly with

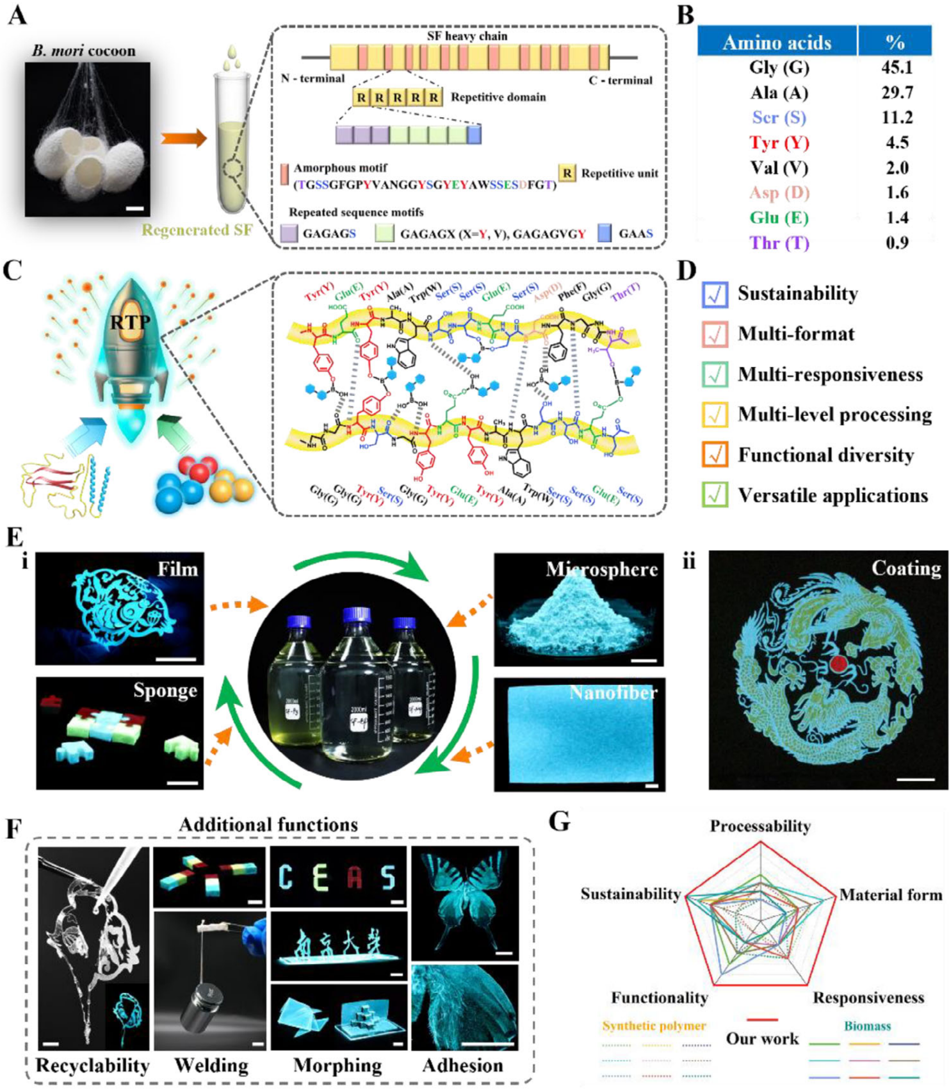

Amino acids	%
Gly (G)	45.1
Ala (A)	29.7
Ser (S)	11.2
Tyr (Y)	4.5
Val (V)	2.0
Asp (D)	1.6
Glu (E)	1.4
Thr (T)	0.9

Figure 1. Versatile RTP-SF systems. A) Schematic diagram illustrating the primary structure of the *Bombyx mori* SF heavy chain. The yellow and red modules represent the unique arrangements of 12 repetitive and 11 amorphous domains, respectively. The amino acid sequence for one of the crystalline and amorphous domains is given to highlight the chemically active amino acids with functional groups. Scale bar: 1 cm. B) The main amino acid compositions of regenerated SF. C) Schematic illustration of forming B—O covalent and hydrogen bonds between SF and arylboronic acids for RTP emission. D) The favorable features of the developed RTP-SF platforms. E) Photographs showcasing RTP-SF materials in different forms, including film, sponge, microsphere, and nanofiber (i), all of which are recyclable and re-processible, and a multicolor patterned coating inkjet-printed on paper (ii). If not otherwise indicated, the RTP images were captured 0.1 s after turning off the UV light. Scale bars: 2 cm. F) Additional favorable functionalities. i) A patterned RTP-SF film partially dissolved by water. Inset: corresponding RTP image. ii) Welded RTP sponges with different color combinations. iii) RTP-SF films with various 3D configurations. iv) An RTP butterfly specimen with an enlarged image showing the phosphorescence details. Scale bars: 1 cm. G) Radar chart comparing the comprehensive value of RTP-SF with other RTP materials based on synthetic polymers and biomass using five indicators. The scoring criteria for the scale are elaborated in Text 1 (Supporting Information) and the plot's Source Data are provided in Tables S1 and S2 (Supporting Information).

diverse solution processing techniques (Figure 1E; Figures S1–S5 and Movie S1, Supporting Information). These RTP platforms exhibit optical stability under ambient conditions while showing the capacity to sense and transform external stimuli into specific optical responses, stemming from the inherent variability of SF in response to diverse external physical and chemical perturbations (see below for details). Furthermore, the water-based self-assembly at ambient temperature and pressure facilitates seamless integration with various multi-scale biomanufacturing techniques, enabling the realization of diversified incorporation of phosphorescent function with other functional elements.

Benefiting from the unique structural properties of SF, the RTP platforms exhibit a range of exceptional functionalities, including water-based recyclability, robust weldability, versatile morphing capacity, and universal adhesiveness (Figure 1F). The platforms can be readily recycled using water as a medium (Figure 1E; Movie S2, Supporting Information), capitalizing on the high solubility of SF in its amorphous state (Figure S6, Supporting Information).[48] For instance, flowing water droplets can rapidly dissolve a patterned RTP-SF film (Figure 1F-i). The resulting aqueous solution can then be reprocessed to enable desired shapes, forms, and functions. When water mist is used instead of liquid water, this dissolution process imparts exceptional weldability.[49] In this process, water molecules disrupt hydrogen bonds within and between protein chains, allowing new entanglements and hydrogen bonds to form when external forces are applied to bring two separate modules together. As the water evaporates, the welding process is completed, leading to the seamless and stable integration of the modules. As shown in Figure 1F-ii, RTP sponges of different colors can be welded together, forming structures capable of supporting loads of at least 600 times their weight (Figure S7, Supporting Information). In addition, the standout morphing capability of silk film, stemming from its ability to induce controllable plastic deformation through the rearrangement of molecular chains under water vapor treatment,[50] enables the 2D RTP structures to transform into various 3D configurations by dint of origami or kirigami techniques (Figure 1F-iii; Figures S8, S9 and Movie S3, Supporting Information). Furthermore, the inherent adhesion properties of SF allow it to form stable and versatile RTP coatings on substrates with various types, textures, and topographies (Figure 1F-iv; Figures S10, S11, and Movie S4, Supporting Information).

The convergence of these remarkable material characteristics within a single platform makes RTP-SF materials highly promising for a broad spectrum of applications. In particular, SF's inherent environmental friendliness, biocompatibility, and biodegradability prevent environmental pollution while establishing a favorable interface with the human body, thereby significantly advancing the development of RTP-SF materials in bio-related scenarios.[37] Compared with RTP systems constructed from petroleum-based polymers or other bio-masses, our RTP-SF platforms offer advantages in terms of comprehensive factors, including material format, processability, stimulus responsiveness, functionality, and sustainability (Figure 1G; Tables S1 and S2, Supporting Information).

2.2. RTP Performance and Molecular Mechanism for Ultralong Phosphorescence

The photophysical properties of multicolor RTP-SF materials were systematically investigated based on SF-Bp-B, SF-Nap-B, and SF-Py-B films (**Figure** 2A–C; Figures S12, S13, Supporting Information). The UV-Vis absorbance spectra of all these films exhibit optical absorbances in the 200–400 nm (Figure S12, Supporting Information). Upon exposure to UV light, all the RTP-SF films emit a faint blue fluorescence. Following the cessation of UV light, they all display pronounced afterglows, with the color shifting from blue to green and then to red in the order of SF-Bp-B, SF-Nap-B, and SF-Py-B films (Figure 2A). Both fluorescence and phosphorescence emissions demonstrate a redshift, attributed to the extended π-conjugation of the arylboronic acids from biphenyl to naphthyl and then to pyrene. As shown in Figure 2B, the fluorescence emission bands shift progressively from 323 to 338 and 389 nm, while the phosphorescence emission bands transition from 475 to 525 and 612 nm. Time-resolved emission decay curves indicate that the RTP-SF films exhibit long-lasting and stable afterglow emission. The SF-Bp-B film demonstrates the longest RTP lifetime, reaching up to 233 ms (Figure 2C). After switching off the UV lamp, the blue afterglow remains visible to the naked eye for up to 9 s, marking one of the highest levels of biomass-based RTP materials.[27,28,51] The RTP lifetime decreases as the π-conjugation extends, with the SF-Nap-B and SF-Py-B films exhibiting lifetimes of 164 ms and 44 ms, respectively. However, the corresponding quantum yield increases, ranging from 2.56% for SF-Bp-B to 4.5% for SF-Nap-B and 12.32% for SF-Py-B. In addition, the excitation-dependent RTP emission could be observed for SF-Nap-B and SF-Py-B films due to the partial formation of aggregates (Figure S14, Supporting Information).[16]

We systematically investigated the underlying mechanism for the RTP-SF. First, we observed that the phosphorescence emission spectrum of a pure SF film exhibits minimal overlap with the absorbance spectra of arylboronic acids, while the afterglow intensity of RTP-SF is significantly higher than that of pure SF (Figure S15, Supporting Information). This indicates that Förster resonance energy transfer between SF and arylboronic acids is negligible.[52] Second, in the absence of alkali involved in the reaction system, the RTP effect is markedly diminished, suggesting that the prolonged RTP effect of RTP-SF primarily results from the alkali-catalyzed covalent coupling between SF and arylboronic acid. Nuclear magnetic resonance (NMR) spectroscopy revealed new ^{1}H resonances at 8.2 ppm and within the 7–8 ppm range assigned to the aromatic hydrogen atoms of arylboronic acids in the ^{1}H NMR spectrum of SF-Bp-B (Figure 2D). These resonances exhibit shifts compared to the arylboronic acid alone. Additionally, the ^{1}H resonance at 5.4 ppm, corresponding to the Ser hydroxyl group, decreases in intensity. Solid-state ^{13}C NMR analysis shows enhanced ^{13}C resonance signals for C_g and C_d in Tyr at 127 ppm following the reaction (Figure 2E), likely due to the proximity of these shifts to those of C_2-C_6 and C_8-C_{10} in bonded biphenylboronic acid (Figure S16, Supporting Information). These observations collectively confirm the occurrence of the B—O covalent reaction between arylboronic acids and SF. It is worth noting that the NMR sample solution was dialyzed to remove unreacted arylboronic acid molecules, eliminating their interference with the test results (Figure S17, Supporting Information). Amino acid analysis results reveal that following the reaction, the levels of Asp, Thr, Ser, Glu, and Tyr—each containing hydroxyl or carboxyl group in the side chain—reduced by 8.77 ± 1.73%, 7.15 ± 3.61%, 7.56 ± 1.83%, 14.95 ± 0.43%, and 5.71 ± 0.31%, respectively (Figure 2F), indicating that these active amino acid residues are involved in covalent bonding reactions. Furthermore, the reaction yields were calculated to be 57.19%, 52.79%, and 55.13% for SF-Bp-B, SF-Nap-B, and SF-Py-B, respectively (Figure S18, Supporting Information).

To further elucidate the interactions between arylboronic acids and SF, we constructed a molecular model of Bp-B and a protein model comprising two types of SF chains, followed by molecular dynamics simulations (Figure 2G). The simulation results confirm the formation of B—O covalent bonds between Bp-B molecules and target amino acids, in agreement with experimental amino acid analysis data. Beyond covalent bonding, extensive hydrogen bonding networks form between Bp-B molecules and SF chains, and energy calculations further reveal

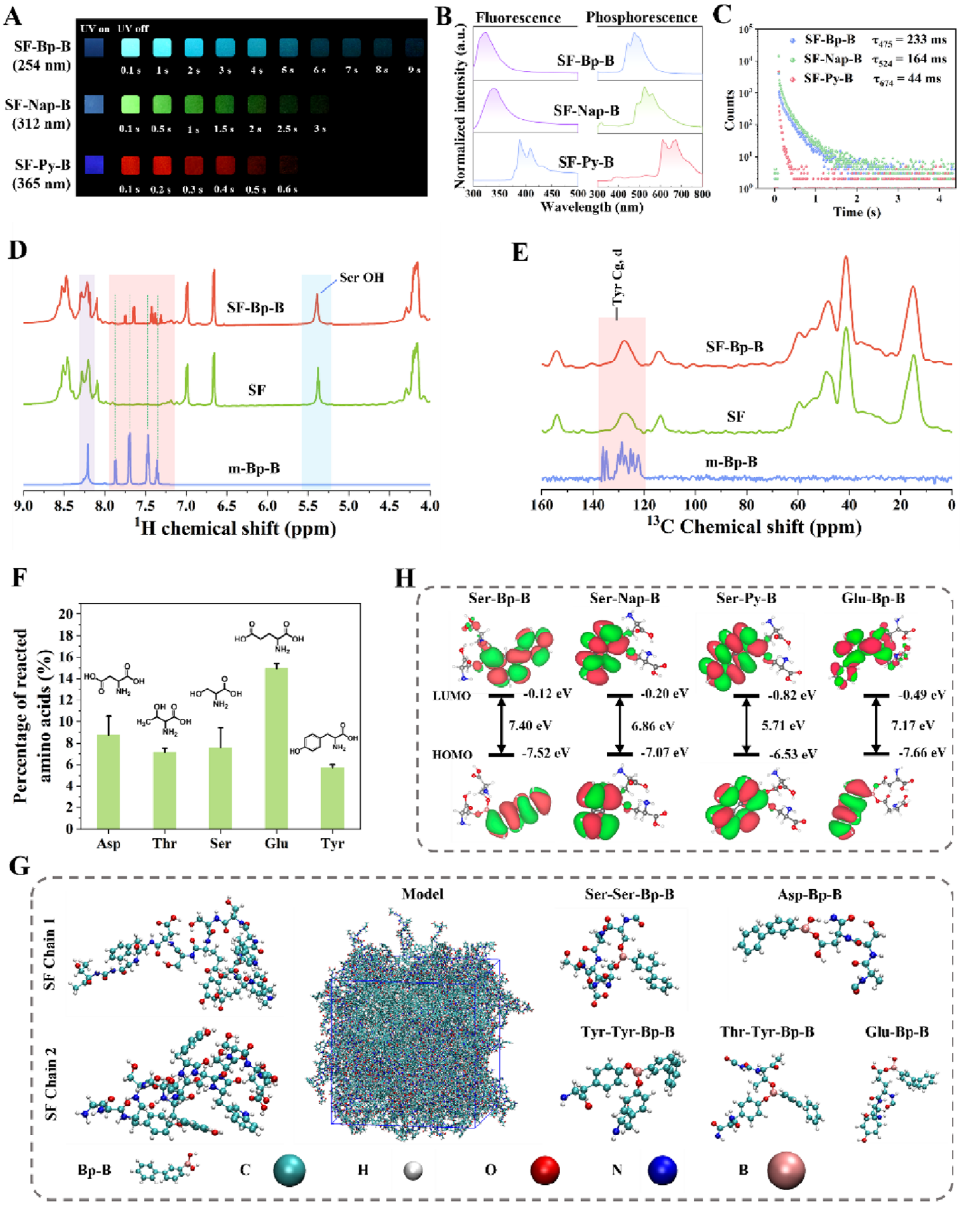

Figure 2. Photophysical properties and mechanism investigations of RTP-SF materials. A) Photographs of SF-Bp-B (λ_{ex} = 254 nm), SF-Nap-B (λ_{ex} = 312 nm), and SF-Py-B (λ_{ex} = 365 nm) films taken upon turning on and off the UV lamp. B) Corresponding steady-state photoluminescence spectra and phosphorescence spectra. C) Time-resolved emission-decay profiles under room temperature. Inset: Phosphorescence lifetimes. D) ^{1}H NMR spectra of regenerated SF and SF-Bp-B in DMSO-d_6/LiCl and m-Bp-B in DMSO-d_6. E) Solid-state ^{13}C CP-MAS NMR spectra of regenerated SF, SF-Bp-B, and m-Bp-B. F) The amino acids involved in the B-O covalent reaction identified by amino acid analysis. Asp: aspartic acid; Thr: threonine; Ser: serine; Glu: glutamic acid; Tyr: tyrosine. G) Molecular dynamics simulation of the covalent linkage between Bp-B molecules and SF chains. Two types of SF molecular chains (SF chain 1 and SF chain 2) with amino acid compositions identical to those shown in Figure 1C were constructed to build the protein model, each comprising 50 chains. H) Frontier molecular orbitals, their respective energy levels, and the energy gaps of Ser-Bp-B, Ser-Nap-B, Ser-Py-B, and Glu-Bp-B. HOMO: highest occupied molecular orbital; LUMO: Lowest Unoccupied Molecular Orbital. Unlike Ser, which forms a C—O—B bond, Glu is linked through a boronic acid ester bond. Data in (F) are presented as mean ± SD, $n = 5$.

substantial contributions from both electrostatic interactions and van der Waals forces to the overall binding energy (Figure S19, Supporting Information). Based on the simulation results, we propose that the formation of stable B—O covalent bonds, hydrogen bonding, electrostatic interactions, and van der Waals forces between arylboronic acids and SF effectively restricts molecular motion and inhibits the non-radiative decay of excited triplet excitons, thus facilitating long-lived RTP. To gain a deeper understanding of the RTP mechanism, we conducted density functional theory calculations. Covalent models of bonding Ser with Bp-B, Nap-B, and Py-B were constructed (Figure 2H). The results reveal that increasing π-conjugation reduces the HOMO-LUMO gaps and the lowest triplet (T_1) energy level, shifting RTP emissions from blue to green, and then red.[4,28] Meanwhile, as the

T_1-S_0 energy gap decreases (Figure S20, Supporting Information), the nonradiative transition of triplet excitons increases, leading to a shorter RTP lifetime. Moreover, a covalent model bonding Glu with Bp-B shows slight variations in the HOMO-LUMO gap and the T_1 energy level, compared to Ser bonded with Bp-B. This subtle difference further supports that the arylboronic acid chromophore, with π-conjugation, plays a crucial role in the RTP emission of RTP-SF.

2.3. Multi-Stimulus Responsiveness

The capacity to trigger molecular rearrangement of SF by UV light and water/methanol molecules,[53] together with the ability to modulate the molecular motion of chromophores by heat, enables the creation of dynamic RTP-SF that can respond to multiple environmental stimuli (**Figure 3A**), enhancing the functionality and versatility of the final RTP platforms in practical applications.

Deep UV light (254 nm) can trigger the breakage of the peptide chains and photodegradation of SF (Figure 3B), resulting in molecular mobility and rearrangements of the SF chains. Therefore, prolonged UV exposure irreversibly disrupts the rigid environment supporting the chromophores, permanently reducing RTP emission. Additionally, when the UV light wavelength matches the chromophores' absorption band, extended UV exposure causes chromophore quenching (Figure 3B), further diminishing the RTP emission in the exposed regions. To verify these statements, we investigated the effects of strong UV exposure at different wavelengths on the afterglow emission of RTP-SF films. As shown in Figures 3C and S21 (Supporting Information), the RTP intensity of all three films gradually decreases with increasing UV irradiation time at varying wavelengths, with the most pronounced effect observed at 254 nm. Among the films, SF-Bp-B demonstrates the fastest decline in RTP intensity, attributed to Bp-B's strongest 254 nm absorption (Figure S15, Supporting Information), leading to severe quenching. In contrast, SF-Nap-B and SF-Py-B films experience milder decreases under 312 nm and 365 nm irradiation, respectively, mainly due to photo-quenching of the chromophores. This behavior enables the patterning of RTP silk films using 254 nm UV irradiation with a shadow mask, exemplified by the "two dragons playing with pearls" pattern (Figure 3A-i,D, left). Furthermore, due to the limited penetration depth of UV light, we can photo-write non-interfering patterns on both sides of the same film, as demonstrated by the butterfly and cherry blossom (Figure 3D, right). Notably, this patterning information remains invisible under visible and UV light (Figure S22, Supporting Information), enabling enhanced anti-counterfeiting capabilities.

Water or methanol molecules interact with the polar groups of the fibroin chains, disrupting hydrogen bonding and promoting chain mobility, thereby compromising the rigid environment necessary for RTP emission (Figure 3E). To explore this, we examined the RTP behavior of SF-Bp-B films subjected to water and methanol vapor. Both vapors progressively decrease the RTP intensity, with water vapor causing faster quenching due to its smaller size and higher polarity, which disrupts hydrogen bonds more effectively than methanol (Figure 3F; Figure S23A, Supporting Information). Upon removal from the vapor, the RTP emission of the film is restored due to the re-establishment of hydrogen bonding interaction between SF-Bp-B chains. Consequently, the RTP properties can be modulated through alternating cycles of vapor fumigation and drying, and the cycle can be repeated multiple times (Figure S23B, Supporting Information). The kinetics of this cycling process can be influenced by the permeation and evaporation rates of vapor within the film, allowing precise timing of RTP emission disappearance and recovery. To demonstrate this, we applied a patterned poly (methyl methacrylate) (PMMA) hydrophobic nanocoating to the RTP-SF film (Figure 3A-ii). This strategy allows for localized regulation of vapor permeation/evaporation rate from the coated side, thus modulating the RTP emission (Figure 3G). The decorated film displays uniform phosphorescence after turning off the UV light. Upon exposure to water vapor, the PMMA nanocoating slows the infiltration rate, leading to delayed luminescence quenching in the coated area, revealing the encoded pattern. As vapor exposure continues, water molecules progressively infiltrate the PMMA-coated regions, gradually decreasing phosphorescence until the pattern disappears. After vapor removal, the PMMA nanocoating also slows the evaporation rate, delaying phosphorescence recovery in the coated area and revealing a reverse image of the original pattern. Ultimately, the pattern vanishes as the water fully evaporates, and the film returns to a uniform phosphorescent color. This strategy of generating encoded patterns through vapor fumigation presents a novel approach for high-security encryption and anti-counterfeiting.

The water responsiveness of the RTP-SF platform enables the modulation of RTP emission by controlling water molecule absorption, facilitated by incorporating a highly hygroscopic substance, like glycerol. As illustrated in Figure 3H, water molecules trapped by glycerol disrupt the hydrogen bonds between SF-Bp-B chains, weakening the rigid environment for optimal RTP emission. Investigating the impact of glycerol concentrations on the RTP emission across different humidity environments, we observed that the intensity gradually decreases with increasing glycerol content at constant humidity (Figures 3I and S24 A, B, Supporting Information). Similarly, the RTP emission diminishes with rising ambient humidity for a fixed level of glycerol addition. This tunability enables the reversible concealment and display of RTP patterns in response to humidity changes (Figure 3A-iii). As illustrated in Figure 3J, the SF-Bp-B film (30 wt.% glycerol) with a UV-written rabbit pattern exhibits no RTP emission at 50% RH; however, the pattern becomes visible when the humidity drops to 30% RH.

RTP-SF also exhibits a temperature-dependent emission because of the thermal deactivation of triplet excitons.[25] Elevated temperature increases the molecular motion of bonded phosphors (Figure 3K), reducing afterglow intensity and accelerating decay. Upon cooling back to room temperature, the RTP properties revert to their initial state. We analyzed the thermal response behavior of RTP-SF films and compared it with the RTP polyvinyl alcohol (PVA) films, which are commonly used in organic RTP platforms.[54] RTP-SF demonstrates slower thermal quenching than RTP-PVA films with the same chromophores (Figures 3L and S25A, Supporting Information). This difference is primarily attributed to the higher glass transition temperature of SF (200 to 220 °C)[32] compared to PVA (≈85 °C). In the case of PVA, elevated temperatures not only inactivate chromophores but also

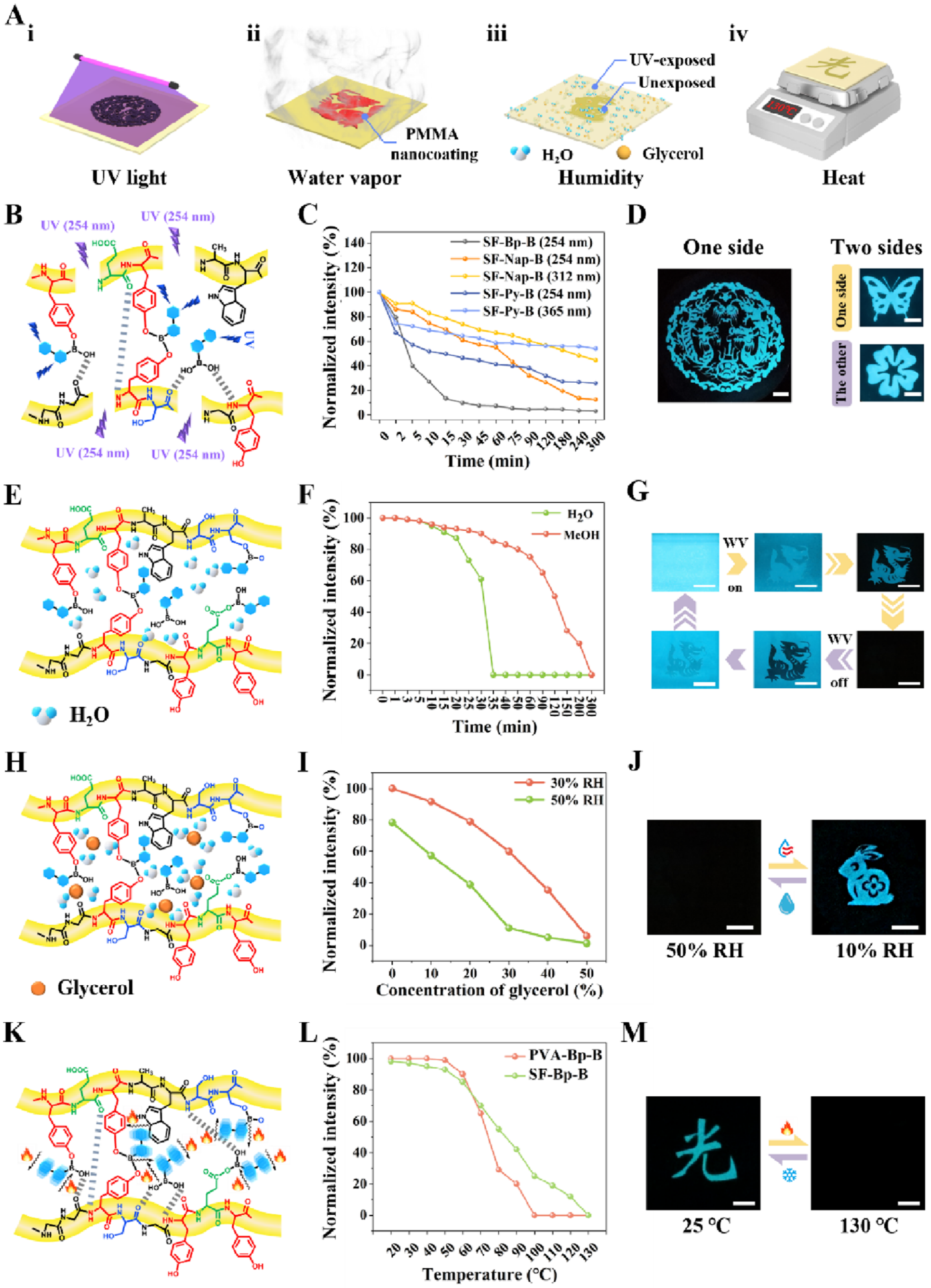

Figure 3. Multi-stimulus responsive capabilities of RTP-SF materials. A) Schematic illustration of the responsiveness of RTP silk to various stimuli: i) UV light; ii) water vapor (WV); iii) humidity; and iv) heat. B–D) RTP property changes induced by UV exposure. B) Schematic showing the changes in molecular structures of SF-Bp-B under UV stimulus. C) Dependence of normalized RTP intensity on UV irradiation time. D) Photographs of RTP patterns on one or both sides of SF-Bp-B films obtained by exposing masked films to UV light. E–G) Reversible RTP property evolution induced by WV exposure. E) Schematic showing the interaction between SF-Bp-B and water molecules. F) Time dependence of RTP intensity under saturated water or methanol vapor treatment. G) Photographs showing the display and concealment of a dragon pattern during continuous WV fumigation and drying. H–J) Reversible RTP property evolution induced by moisture treatment. H) Schematic of the interaction between glycerol-doped SF-Bp-B and water molecules. I) Dependence of RTP intensity on glycerol concentration under varying humidity levels. J) Photographs showing the display and concealment of a UV-written rabbit pattern on a glycerol-doped (30% w/w) SF-Bp-B film during the moisturizing and drying. K–M) Reversible RTP property evolution induced by heat treatment. K) Schematic showing the interaction between SF-Bp-B and heat stimulus. L) Normalized RTP intensity of SF-Bp-B and PVA-Bp-B films as a function of temperature. M) Photographs showing the responsive behavior of a UV-written “光” pattern to heat treatment. Scale bars in D, G, J, M: 1 cm.

break the rigid environment that supports the chromophores due to the induced glass transition, resulting in a sharp decrease in RTP intensity. Leveraging the reversible temperature responsiveness of RTP-SF (Figure S26B, Supporting Information), reversible pattern display and concealment can be achieved. For instance, a "光" pattern on an SF-Bp-B film vanishes at 130 °C and reappears upon cooling to room temperature. In contrast, lowering the temperature from room temperature causes a gradual increase in RTP intensity (Figure S27A,B, Supporting Information). This enhancement arises because low temperatures suppress non-radiative transitions while radiative transitions remain largely unaffected, thereby increasing the luminescence quantum yield.

In addition, we investigated the responsiveness of RTP-SF films to combined stimuli such as high humidity and high temperature, UV exposure, and high temperature. The results demonstrate clear synergistic interactions among humidity, temperature, and UV irradiation, which significantly enhance their regulatory influence on RTP emission (Figures S24, S25, and S28, Supporting Information). Notably, analysis of the response stability of RTP-SF films under simultaneous high-humidity and high-temperature conditions indicates that such combined stimuli do not compromise the material's stimulus-response stability (Figures S23C and S26, Supporting Information). Furthermore, we examined the long-term stability of RTP-SF films under complex environmental conditions. The results demonstrate that the films maintain good stability in high-humidity environments (75% RH for 1 month), during short-term high-temperature exposure (150 °C for 48 h) and long-term low-temperature storage (−80 °C for 3 weeks), and after immersion in common organic solvents (ethanol, acetone, and isopropanol) for 48 h (Figures S27C and S29, Supporting Information). In contrast, prolonged exposure to 150 °C or intense sunlight results in a significant decline in RTP intensity. Fourier-transform infrared spectroscopy (FTIR) results further confirm that the reduction in RTP intensity primarily arises from the irreversible quenching of the phosphors by heat and UV components of the solar spectrum, rather than from structural changes in the material (Figure S30, Supporting Information). These findings highlight that, for practical applications, extended exposure to elevated temperatures or intense sunlight should be avoided to ensure the long-term preservation of their RTP performance.

2.4. Multi-Mode Processability and Multidimensional Integrability

RTP-SF is highly compatible with ink-based processing owing to its favorable solution properties (Figure S31, Supporting Information), providing flexibility in creating diverse complex structures, forms, and architectures. Moreover, water-based processing offers a more sustainable approach, reducing the environmental impact of traditional manufacturing methods that necessitate harsh solvents or chemicals while maintaining high-quality outputs. A broad spectrum of ink-based micro- and nanopatterning techniques—such as spray coating, screen printing, stamp printing, and inkjet printing—can transform aqueous RTP-SF solution into patterned phosphorescent structures (Movie S5, Supporting Information). These techniques enable the creation of multicolored, intricate, and high-resolution designs applicable to a wide array of substrates. Of particular significance, the exceptional adhesiveness of the processed coatings ensures the durability and reliability of RTP patterns in real-world applications. In addition, the RTP-SF ink demonstrates excellent physical and long-term storage stability (Figure S32, Supporting Information), showing no significant changes in rheological properties after 24 h of ultrasonication, 1 week of rocking-bed shaking, and 6 months of storage at ambient conditions (20–30 °C). **Figure** 4A highlights the multi-mode processing capabilities of RTP-SF ink.

Using RTP-SF ink, we first demonstrate its capability to generate RTP patterns via spray coating (Figure 4A-i). This approach allows for the easy formation of phosphorescent coatings on substrates of varying types and topographies (Figures S10,S11, Supporting Information). Figure 4A-i displays the phosphorescent Chinese characters sprayed onto ginseng using SF-Nap-B ink. Owing to the thin nature of the phosphorescent coating, its fluorescence is faint under UV illumination, with no fluorescence visible (Figure S33 , Supporting Information). However, when the UV light is turned off, the "参" pattern becomes visible through yellow phosphorescence. Screen printing offers an effective approach for large-scale RTP pattern fabrication. As shown in Figure 4A-ii, we screen-printed the green RTP motto of Nanjing University on a cloth bag. Furthermore, the RTP ink can be applied to a raised surface of a stamp to execute stamp printing (Figure 4A-iii). For instance, a "福" pattern was successfully printed onto a human arm. Last, the RTP ink can be integrated with high-throughput inkjet printing technology to construct high-resolution, multicolor phosphorescent patterns (Figure 4A-iv), as demonstrated by printed patterns on paper, including an introductory article about Nanjing University (Figure S34, Supporting Information), butterfly designs, and a color rendition of Van Gogh's self-portrait. The compatibility with diverse solution-based patterning techniques greatly enhances the versatility of RTP-SF inks for a broad array of applications (Movie S6). For example, Figure S35 (Supporting Information) depicts a Statue of Liberty RTP pattern integrated onto a dollar bill using inkjet printing for secure labeling. Additionally, a dual-level anticounterfeiting system can be established by adding a layer of fluorescent information (Figure S36, Supporting Information), further elevating the security level.

Furthermore, the RTP-SF platforms can be post-processed using advanced manufacturing techniques to fabricate integrated, multidimensional optical systems, rendering them highly promising for high-security anti-counterfeiting and encryption applications. Combining different functional elements in a single platform makes it possible to generate highly intricate, layered security features that are difficult to replicate, tamper with, or decrypt. These capabilities are demonstrated through the utility of the integrated platform for multilevel anti-counterfeiting, multistage encryption, and 3D encryption.

A multilevel anti-counterfeiting system was first developed, incorporating three security layers, facilitated by integrating physical structural color and chemical phosphorescent color. Physical structural color is enabled by SF's ability to form periodic photonic nano-architectures via a water vapor-assisted imprinting technique.[50] The preparation of this triple-layered anticounterfeiting system is illustrated in Figure S37(Supporting

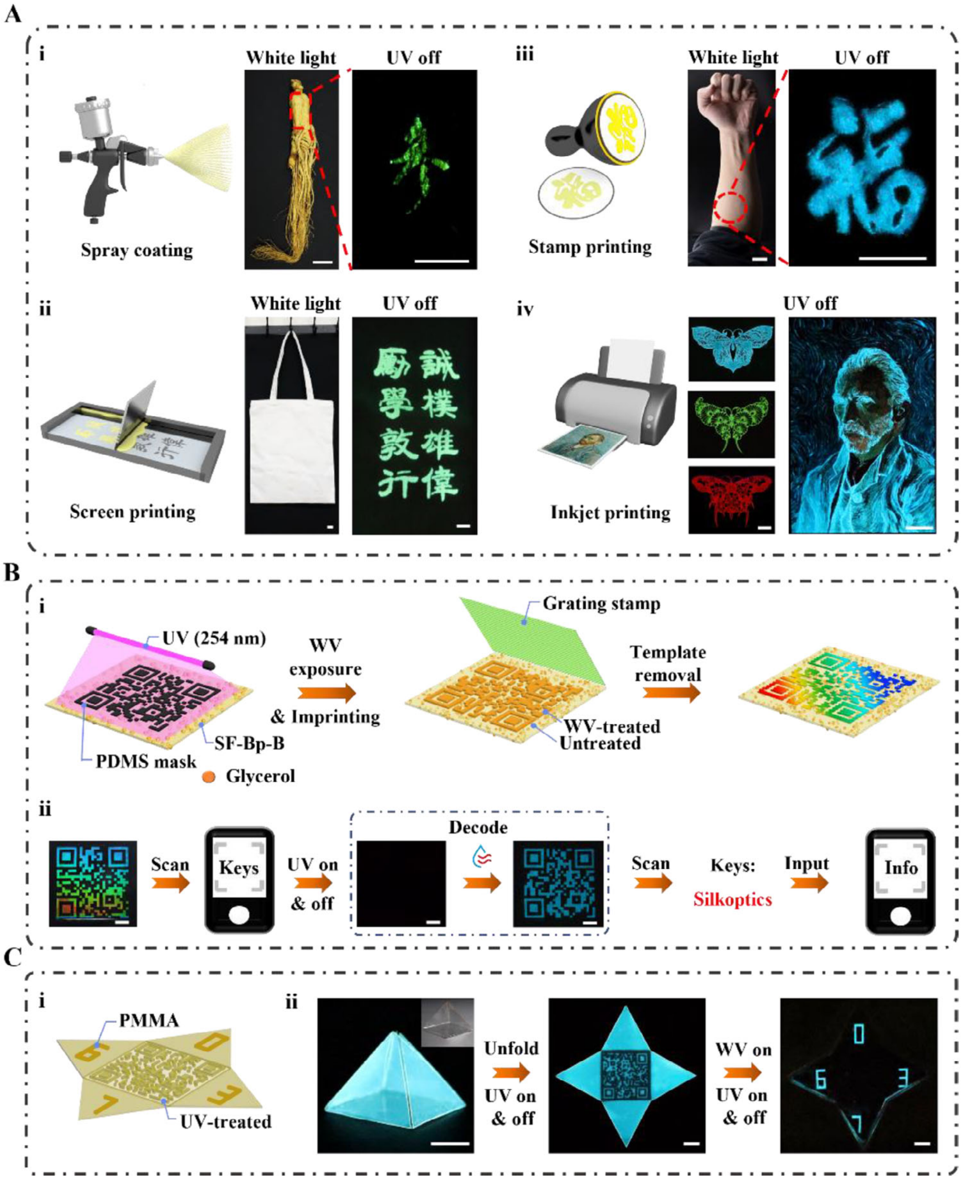

Figure 4. Multi-mode processing and multidimensional integration of RTP-SF materials. A) Formation of phosphorescent patterns using multiple processing methods with RTP-SF inks. i) A "参" pattern sprayed on ginseng; ii) The Nanjing University's motto screen printed on a fabric bag; iii) A "福" pattern stamp printed on the arm; iv) Various high-resolution patterns inkjet printed on paper: three butterfly patterns (left), and Van Gogh's self-portrait (right). The patterns can only be identified after switching off the UV light. Scale bars: 2 cm. B) i) Schematic of the preparation process for a high-level encrypted QR code by decryption with drying-triggered phosphorescence. ii) Decryption process of encrypted QR code: deciphering the encrypted keys to the structural color code through drying and after stopping UV light exposure. Scale bars: 1 cm. C) Schematic (i) and photographs (ii) of a pentahedron-shaped multilevel encryption platform that combines reconfigurable architecture and responsive phosphorescence. Inset: the pentahedron under white light. Scale bars: 2 cm.

Information) and described in the Methods. The structural color layer ("南京大学", Level I), visible in daylight at a specific direction, offers an iridescent element that shifts in appearance based on the viewing angle (Figure S38, Supporting Information). The RTP information, displayed on both sides of the film under dark conditions, represents the second ("North Building of Nanjing University," Level II) and third ("Library of Nanjing University", Level III) security layers. Next, this system provides an innovative approach for multistage encryption by combining structural color with concealable phosphorescent color (Figure 3G,J). One effective strategy leverages the humidity-responsive properties of the RTP-SF platform doped with glycerol. As proof of concept, we created an encrypted QR code using a glycerol-doped SF-Bp-B film (Figure 4B). Two steps are required to decode the encrypted information: i) extracting the structural color QR code under specific visible light angles; ii) drying the film to reveal the hidden phosphorescent QR code, unlocking the "Silkoptics" key to the structural color code and fully accessing the encoded message.

Lastly, the capacity to transform 2D structures into 3D shapes (Figure 1F) enables the creation of 3D RTP encryption architectures by integrating 2D encoded RTP films with origami techniques. To validate this concept, we developed a pentahedron-shaped, triple-encrypted 3D device that integrates the vapor-induced RTP display—imparted by PMMA nano-coatings—with a 3D configuration (Figure 4C). The fabrication process is described in detail in the Methods section, and the corresponding precursor structure is illustrated in Figure 4C-i. After folding, the pentahedron reveals no information under visible light or after UV light cessation. To decode, the pentahedron must first be unfolded (1st encryption layer). Subsequently, UV excitation reveals the QR code (2nd encryption layer), which leads to the key input page. Upon water vapor exposure, the key "0367" becomes visible once UV excitation ceases (3rd encryption layer), granting access to the encrypted message. These anti-counterfeiting and encryption frameworks demonstrate the capacity of RTP-SF platforms to support robust, high-level protection for diverse secure information systems through simple and cost-effective manufacturing techniques.

2.5. Multifunctional RTP-SF Platforms for Sustainable Electronic Interfacing

Our RTP-SF platforms demonstrate multifunctional capabilities, enabled by their multi-responsiveness, multi-scale processing capabilities, and ease of functionalization. The platform's inherent RTP emission not only encourages its use in information anti-counterfeiting and encryption but also allows for the incorporation of sensing capabilities, driven by its controllable and reversible stimulus responsiveness. Beyond, as mentioned above, the integration of photonic nanostructures onto the surface of the RTP-SF matrix imparts structural color, enhancing its functionality for visualizing-related applications. What's more, aqueous solution-based processing facilitates the incorporation of functional components, strengthening the platform's versatility. These features, combined with the inherent recyclability of the RTP-SF platform, offer a promising pathway toward advanced sustainable applications. To exemplify these advantages, we demonstrate its applicability in electronic interfaces and showcase its potential to address key challenges in electronics.

The rise in counterfeit electronics threatens their reliability and safety, making advanced anti-counterfeiting measures essential.[55] Additionally, ensuring electronic components stay within their optimal operational temperature range is vital to prevent performance degradation and failure. To tackle these issues, we developed a multifunctional labeling system that integrates display, anti-counterfeiting, and temperature-sensing functionalities for electronic component authentication and monitoring (**Figure** 5A–D). The labels display the trademark security pattern of "*SSO*" under visible light and the phosphorescent security pattern of "*CPU*" after stopping UV excitation (Figure 5A). These labels can be firmly attached to the computer motherboards using a water vapor fumigation approach (Figure 5B,C), thus providing durable identification and temperature monitoring. By integrating a UV light source and an on/off controller into the computer, real-time monitoring and recording of RTP signals becomes possible. As shown in Figure 5D, the "*CPU*" pattern's intensity progressively diminishes with rising temperature, becoming undetectable above 120 °C. Upon cooling, the RTP intensity fully restores. This temperature-dependent RTP signal enables real-time monitoring of integrated circuit temperatures, ensuring stable component operation. Notably, SF's excellent infrared radiation performance[56] minimizes any additional heat burden on integrated circuits, further enhancing the RTP platform's benefits.

Furthermore, the complex architecture of electronic products has substantially hindered the separation and recycling of electronic waste (e-waste), leading to elevated treatment costs and the frequent disposal of e-waste through landfilling or incineration.[57] These practices pose severe environmental pollution, resource depletion, and direct threats to human health. As such, endowing these multifunctional labels with excellent chemical recyclability and reprocessability is of great importance for advancing sustainable electronics management. As shown in Figures 5E and S39 (Supporting Information), the label can be completely dissolved in water within 120 s after usage, thanks to the water solubility of the RTP-SF matrix assembled in its amorphous state. The resulting RTP-SF solution can be reprocessed through direct casting, which enables the formation of a novel multifunctional label after reprogramming its structural color and phosphorescence. Evaluated by FTIR and phosphorescence spectral analysis (Figure 5F,G), the recycled labels exhibit consistent structures and RTP properties compared to the original label, even after five recycling cycles, indicating the preservation of the conformations and interactions between arylboronic acids and SF during recycling and reprocessing. The recycling rate test indicates that after five cycles, the RTP-SF labels retain 91.6 ± 1.91% of their initial quality (Figure S40, Supporting Information), confirming their excellent recyclability. We further evaluated the actual environmental degradability of multifunctional optical labels by burying a sample in a humid soil at a depth of 2 cm and maintaining it at room temperature. Morphological changes were monitored over time. As depicted in Figure 5H, the label undergoes a gradual disintegration process within 60 days, attributed to microbial activity capable of directly attacking and digesting the SF chains, thereby confirming the outstanding sustainable utility of RTP-SF materials.

2.6. Biocompatible RTP-SF Platforms for Biomedical Interfacing

The inherent biological attributes of SF endow the developed RTP-SF platforms with strong potential for use as multifunctional interfaces in biomedical applications. To demonstrate this potential, we first assessed the biocompatibility and biodegradability of the RTP-SF platforms. In vitro cytotoxicity of RTP-SF solutions is analyzed by culturing L-929 cells. The cells cultured in RTP-SF solutions exhibit enhanced viability compared to the control (pristine culture medium) after 24 h incubation (**Figure** 6A), demonstrating the material's dual capacity to promote cellular proliferation while maintaining cytocompatibility. Furthermore, fluorescence staining and imaging show minimal dead cells in both RTP-SF and the control groups (Figure 6B; Figure S41, Supporting Information), providing additional evidence for their excellent cytocompatibility. The in vitro degradation results of crystalline RTP-SF films (Figure S42,

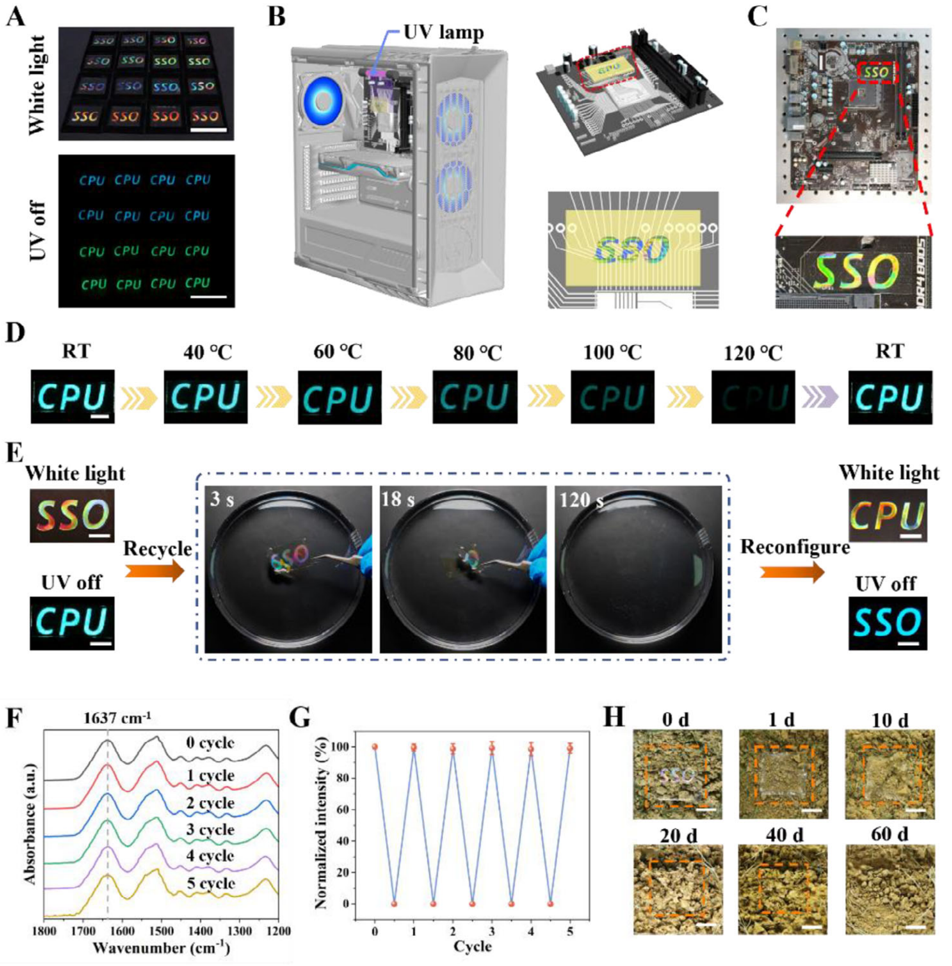

Figure 5. Sustainable utility of multifunctional optical labels. A) A set of multifunctional optical labels that integrate display, anti-counterfeiting, and sensing capabilities. Scale bars: 5 cm. B) Schematics illustrating a multifunctional label applied to the integrated circuit board of a mainframe. C) Corresponding photographs of the label attached to the integrated circuit board, showing the vivid "*SSO*" structural color pattern. D) Photographs depicting the reversible thermo-responsiveness of the "*CPU*" afterglow pattern. Scale bar: 1 cm. E) The recycling and reprocessing of the optical labels. Scale bars: 1 cm. F, G) FTIR spectra (F) and phosphorescence intensity at 475 nm (G) of recycled labels with different recycle times. H) Degradation of the multifunctional optical label in a humid soil environment at room temperature. Scale bars: 2 cm. Data in (G) are presented as mean ± SD, *n* = 4.

Supporting Information) reveal that more than 70% of the film's mass was lost after 30 days of exposure to protease, while control samples incubated in phosphate buffer saline (PBS) solution (pH 7.4) without the enzyme exhibited negligible mass loss (Figure 6C). Notably, the degradation products showed no cytotoxic effects (Figure S43, Supporting Information), further confirming the outstanding biocompatibility of RTP-SF materials. To demonstrate the practical biomedical implications of the RTP-SF platforms, two representative examples—its integration with medicines and face masks—are presented below.

The increasing prevalence of counterfeit and substandard medicines, especially with the rise of online pharmacies, underscores the urgent need for advanced biosafety anti-counterfeiting technologies. Simultaneously, maintaining pharmaceutical storage conditions within optimal humidity ranges is critical for preventing the reduced efficacy, ineffectiveness, or even toxicity of pharmaceuticals resulting from moisture-induced chemical degradation.[58] The multifunctional RTP-SF platforms presented here can confer high-security anti-counterfeiting and real-time humidity monitoring capabilities to medicines. To demonstrate this concept, we fabricated a roll of anti-counterfeiting labels containing "Genuine" patterns, displaying no visible information under normal light, but revealing the RTP information after switching off the UV light (Figure 6D). Such security labels, when applied to products like medication vials, can be combined with the RTP signals applied directly to the medications to provide strong authentication (Figure 6E and Movie S7, Supporting Information). Additionally, the RTP signals on the tablet surfaces can serve as "moisture probes" to monitor the humidity of their storage environments in real time, ensuring optimal quality and stability of the medications throughout the storage. As shown in Figure 6F, the RTP intensity exhibits a progressive decrease with increasing relative humidity, followed by complete recovery upon desiccation.

Face masks are vital for promoting public health, safeguarding personal health, and fulfilling social responsibilities.

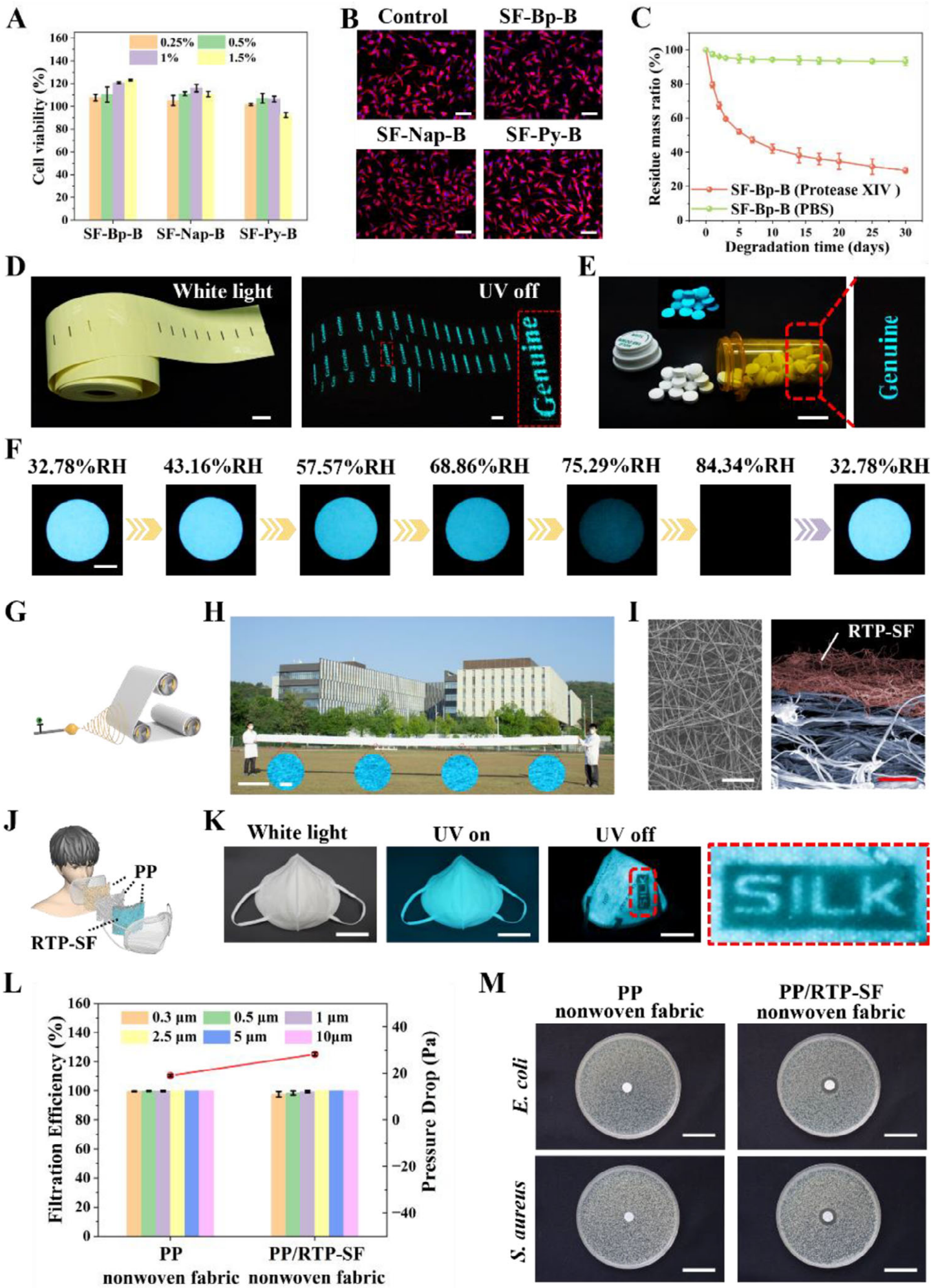

Figure 6. Biomedical applications of multifunctional RTP-SF materials. A) Metabolic activity of cells cultured in media containing RTP-SF solutions of different concentrations after 24 h of culturing. B) Corresponding fluorescent images of cells cultured in different media (RTP-SF solution concentration: 1 wt.%). Scale bars: 50 µm. C) Degradation profiles of SF-BP films in PBS solution and protease XIV PBS solution. D) Formation of a roll of anti-counterfeiting labels through inkjet printing. Scale bars: 2 cm. E) An anti-counterfeiting label affixed to the surface of a medicine bottle with the enlarged image showing the clear "Genuine" pattern. Inset: SF nanofibers-based RTP signals applied onto the surface of the medications via electrospinning. Scale bar: 2 cm. F) Afterglow photographs of RTP tablets exposed to different humidity environments. Scale bar: 1 cm. G) Schematic diagram illustrating the preparation of RTP-SF nonwoven fabric using electrospinning. H) Photograph of a large PP/RTP-SF nonwoven fabric with the enlarged image showing the bright afterglow color. Scale bars: 1 m, 5 mm (inset). I) (left) Surface SEM image of the RTP-SF nonwoven fabric, showing the random nanofibers. (right) Cross-sectional SEM image of the PP/RTP-SF nonwoven fabric, showing the compact combination of two components. Scale bars: 20 µm (left), 50 µm (right). J) Schematic diagram of RTP-SF nonwoven fabric integrated into an N95 mask. K) Photographs of a multifunctional phosphorescent mask under different light conditions. The "SILK" pattern was created via the shadow mask-assisted UV patterning method. Scale bars: 5 cm. L) A comparison of filtration efficiency and pressure drop between PP/RTP-SF and PP nonwoven fabrics. M) Antibacterial properties of PP/RTP-SF and PP nonwoven fabrics evaluated through an inhibition ring experiment. Scale bars: 3 cm. Data in (A), (C), and (L) are presented as mean ± SD, (A) $n = 5$, (C) $n = 4$, (L) $n = 4$.

Standards-compliant masks can effectively block the transmission of pathogens, protecting respiratory health. However, counterfeit and substandard masks, often made from inferior materials or irregular production processes, pose serious safety hazards and health risks, making anti-counterfeiting essential. Moreover, incorporating antimicrobial materials into face masks enhances their protective efficacy by reducing bacteria or mold growth, especially in high-risk environments.[59] Combining anti-counterfeiting and antimicrobial features in face masks would offer an economical strategy for addressing the complex health and safety challenges. Building on this, we fabricated a multifunctional mask integrating filtration, anti-counterfeiting, and antibacterial properties (Figure 6G–M; Movie S7, Supporting Information). We first created an SF nanofiber layer with both RTP and antibacterial properties on commercial polypropylene (PP) nonwoven fabrics through electrospinning (Figure 6G), by leveraging the ability of SF to act as a bio-template for the in-situ generation of silver nanoparticles (AgNPs) under light exposure.[60] Figure 6H shows the large-scale preparation of the composite nonwoven fabric, with a uniformly distributed surface RTP intensity. Morphological analysis reveals the close contact between the SF nanofiber and PP layers (Figure 6I). By incorporating this composite nonwoven fabric as a functional layer, multifunctional face masks were produced. The mask appears ordinary under visible light. However, when exposed to UV light, it exhibits a uniform blue fluorescence, and upon cessation of UV exposure, a phosphorescent anti-counterfeiting pattern reading “SILK” became visible (Figure 6 J,K). Filtration tests show that the mask maintains over 99% filtration efficiency, and the pressure drop increase (from 19.0 Pa to 28.2 Pa) remains within the standard range for wearing comfort (Figure 6L). The increased pressure drop is attributed to the larger surface area provided by the silk nanofiber layers, which results in higher viscous forces between the fibers and the airflow. Finally, given the significant effect of AgNPs in disrupting the structure of mature biofilms and killing the corresponding bacteria, the composite fabric effectively killed both Gram-negative (Escherichia coli, *E. coli*) and Gram-positive (Staphylococcus aureus, *S. aureus*) bacteria with restricted growth, as evidenced by the formation of an antimicrobial ring (Figure 6M). Antibacterial rate was further measured with values exceeding 99.53% and 99.99% for *E. coli* and *S. aureus*, respectively (Figure S44, Supporting Information). In contrast, the pure PP nonwoven fabric showed no antimicrobial activity, highlighting the enhanced bacterial-killing performance of the composite fabric. This multifunctional face mask improves the safety and efficacy of personal protective products, offering a promising new solution for public health protection.

3. Conclusion

We have successfully demonstrated the potential of versatile SF in developing high-performance RTP systems with varied material formats, multi-mode tunable afterglow, multi-scale processability, and diversified functionalities. Driven by the multiple interactions between the arylboronic acid phosphors and the SF matrix, the resulting RTP-SF platforms exhibit long-lived RTP emission with lifetimes of up to 233 ms. Moreover, these platforms feature water-based formability, controllable recyclability and degradability, and excellent biocompatibility, positioning them as promising candidates for sustainable and biocompatible photoluminescence technologies. Given these superior material attributes, the RTP-SF effectively addresses the key limitations of existing biomass-based RTP systems, enabling a wide array of multifunctional and adaptive applications. In particular, the RTP-SF is uniquely suited for use at the interface of photonics and biological systems. These protein-based RTP platforms hold great potential for real-world utilities, driven by advancements in the large-scale production of RTP-SF, the scaling up of silk material processing, and the ongoing refinement of the relationship between structures, properties, and functionalities within RTP silk systems. The ability to integrate the RTP function with other optical, mechanical, and additional functionalities presents a promising opportunity for developing novel RTP systems with enhanced versatility, adaptability, and intelligence. The outlined strategy of integrating bottom–up chemical modification, top–down manufacturing techniques, and programmable stimulus-responsive behaviors opens a new avenue for developing biomass-based sustainable, biodegradable, intelligent, and multifunctional devices, promoting the broader adoption of biomass materials in advanced photonics technologies.

4. Experimental Section

Materials: *Bombyx mori* silkworm cocoons were purchased from local farmers in Nantong. Ammonium hydroxide ($NH_3 \cdot H_2O$, 25–28%), hydrochloric acid (HCl, 36.0–38.0%), sodium carbonate (Na_2CO_3, 99.5%), and nitric acid silver ($AgNO_3$, 99.8%) were obtained from Sinopharm Chemical Reagent Co., Ltd. Lithium bromide (LiBr, 99%), glycerol (99%), and PBS were purchased from Macklin Biochemical Co., Ltd. 3-biphenylboronic acid (98.75%) was purchased from Bide Pharmatech. 1-naphthylboronic acid (98%), and 1-pyrenylboronic acid (99%) were purchased from Heowns Biochemical Technology Co., Ltd. Methanol (CH_3OH, 99.5%), dichloromethane (CH_2Cl_2, 99.5%), and lithium chloride (LiCl, 99.9%) were all of the analytical grades and purchased from Aladdin Co., Ltd. Dialysis membranes (44 mm, 3500 D) were purchased from Acmec Biochemical Co., Ltd. PMMA (950, A7) was purchased from Suzhou Research Materials Microtech Co., Ltd. DMSO-d6 was purchased from Adamas Co., Ltd. Polydimethylsiloxane (PDMS, Sylgard 184) was purchased from Dow Corning Co., Ltd. Trichloro (^{1}H,^{1}H,^{2}H,^{2}H-perfluorooctyl) silane (97%) was purchased from Xushuo Biotechnology Co., Ltd. Protease XIV from Streptomyces griseus was purchased from Shanghai Yuanye Bio-Technology Co., Ltd. LB broth medium and agar powder were purchased from Sangon Biotech. DMEM cell culture medium, Fetal Bovine Serum (FBS), antibiotic/antimycotic, and AlamarBlue cell viability reagent were obtained from Thermo Fisher. 4′,6-diamidino-2-phenylindole (DAPI) was obtained from Beyotime Biotechnology Co., Ltd, and tetraethyl rhodamine isothiocyanate-phalloidin (TRITC-phalloidin) was obtained from Yeasen Biotechnology Co., Ltd. PP nonwoven cloth (BF99) was purchased from Haorui Tech Co., Ltd.

Preparation of SF Solution: The SF solution was prepared following standard protocols.[61] In brief, raw silk cocoons were first boiled in a 0.02 M Na_2CO_3 aqueous solution for 30 min, followed by thorough rinsing in distilled water to remove the sericin layer. After being dried for 48 h, the degummed silk fibers (2.5 g) were dissolved in 10 mL of 9.3 M LiBr solution at 60 °C for 4 h and then dialyzed against distilled water for 3 days. The post-dialysis solution was subsequently centrifuged at 11 000 rpm for 20 min to attain a 6–7 wt.% SF solution. To obtain a concentrated suspension (12 wt.%), the nascent SF solution was gently blown with a fan, allowing for the slow evaporation of water. To obtain a lower molecular weight aqueous solution of SF for RTP ink processing, the sericin removal process was prolonged to 120 min, while the other steps remained unchanged.

Preparation of RTP-SF Solution: The RTP-SF solution was prepared by adding 12 wt.% SF (3 mL), arylboronic acid (3- biphenylboronic acid (5 mg), 1-naphthyl boronic acid (5 mg), or 1-pyrenylboronic acid (10 mg) in water (4 mL), and ammonium hydroxide (1 mL), followed by stirring the mixture at 80 °C for 20 min. The reacted solution was dialyzed against distilled water for 48 h, resulting in the formation of an RTP-SF solution.

Preparation of RTP-SF Platforms—RTP-SF Films: An RTP-SF film with an approximate thickness of 50 µm was fabricated by casting a specified volume of RTP-SF solution onto a silicon wafer pre-treated with trichloro(^{1}H,^{1}H,^{2}H,^{2}H-perfluorooctyl) silane, followed by drying for 24 h (25 °C, 30–40% relative humidity). To prepare the glycerol-doped film, a glycerol solution with solid content ranging from 10% to 50% was incorporated into the RTP-SF solution before casting it into a film.

Preparation of RTP-SF Platforms—RTP-SF Microspheres: RTP-SF solution was introduced into a spray dryer (B-290, Buchi, Switzerland) at a feed rate of 30%, with the extractor fan operating at full power (100%). The inlet and outlet temperatures were maintained at 150 and 80 °C, respectively. The resulting RTP-SF microspheres were collected from the collection chamber of the spray dryer.

Preparation of RTP-SF Platforms—RTP-SF Sponges: A concentrated RTP-SF solution (12 wt.%) was poured into an acrylic mold and subsequently frozen at −80 °C for 12 h. The RTP-SF sponge was then obtained by lyophilizing for at least 48 h using a freeze dryer (10N/C, Scientz, China).

Preparation of RTP-SF Platforms—RTP-SF Micro-/Nanofibers: RTP-SF micro-/nanofibers were fabricated by electrospinning (DP30, Yunfan Technology, China) using a concentrated RTP-SF solution (15 wt.%) under ambient conditions. An applied voltage of 20 kV and a collector-to-needle distance of 12 cm were used.

Patterning of RTP-SF Platforms—Deep UV Light Patterning: A UV germicidal lamp (G36T5VH, Serve Tool Inc., USA) with a wavelength of 254 nm and a power output of 40 W was employed for UV irradiation. Black shadow masks, designed with specific patterns, were placed on the RTP-SF platforms before UV exposure to selectively quench phosphorescence in the uncovered regions. The distance between the sample and the UV lamp was maintained at 2 cm, and the irradiation duration was set to 0.5 h. Note that the UV intensity used for patterning is much higher than that used for triggering RTP emission.

Patterning of RTP-SF Platforms—Patterned PMMA Nanocoating Preparation: Preparing a layer of patterned PMMA nanocoating on an RTP-SF film involves three steps. First, a layer of PMMA nanocoating was prepared onto a silicon wafer pre-treated with trichloro(^{1}H,^{1}H,^{2}H,^{2}H-perfluorooctyl) silane by spin-coating. Next, the PMMA-coated wafer, covered with a custom-designed PDMS shadow mask, was subjected to oxygen plasma treatment to selectively etch the PMMA nanocoating. Finally, after hydrophobic treatment of exposed areas, an RTP-SF solution was applied to the wafer, filling the patterned PMMA nanocoating regions. After drying and peeling off, a PMMA nanocoating decorated RTP-SF film was obtained. The formed PMMA nanocoating can be erased (through acetone cleaning) and recreated, enabling the rewriting of the encoded pattern information (Figure S45, Supporting Information). To disclose the RTP pattern, the RTP-SF film was put on top of the saturated water vapor (20–25 °C) or heated water surface (≈40 °C) with the PMMA nanocoating-decorated surface directly exposed to water vapor over a controlled time.

Processing of RTP-SF Inks—Spraying Coating: The RTP-SF ink (12 wt.%) was sprayed onto a substrate from a distance of 10 cm using a spray gun. To create a patterned RTP design, a polyethylene mask was applied to the surface of the 3D object before spraying the ink.

Processing of RTP-SF Inks—Screen Printing: After securely positioning a screen stencil onto the surface of a targeted substrate, the poured RTP-SF ink (12 wt.%) was evenly spread at a controlled speed using a squeegee. The ink passes through the open areas of the screen, transferring the design onto the substrate beneath. Afterward, the screen was carefully removed, and the printed substrate was placed in an oven at 60 °C to dry.

Processing of RTP-SF Inks—Stamp Printing: A stamp featuring a design was immersed in a sponge saturated with a 12 wt.% RTP-SF ink and then applied to the targeted substrate. After being evenly pressed, the stamp was removed, allowing the ink to dry naturally under ambient conditions. To prepare the dual-security coating in Figure S45 (Supporting Information), the fluorescent ink was first prepared by mixing commercial fluorescent dyes with SF solution, followed by the sequential printing of the fluorescent ink and SF-Nap-B ink onto the same area of calligraphic rice paper using two custom stamps.

Processing of RTP-SF Inks—Inkjet Printing: Low molecular weight SF (120 min boiling SF) was used to prepare the RTP-SF ink for inkjet printing. RTP-SF inks of different colors, prepared at a concentration of 9 wt.% and a molecular weight of 56 kDa (Figure S46, Supporting Information), were then loaded into the cartridges of a commercial printer (L1258, EPSON, Japan). After purging the air, the ink was printed onto conventional paper or other substrates.

Processing of RTP-SF Inks—Micro-/Nanoimprinting: Micro-/nanoimprinting was performed using the previously reported method.[50] In brief, an RTP-SF film was placed on a clean PDMS substrate and exposed to water vapor at 45 °C for 30 s. A grating master with a period of 800 nm was then applied to the wetted film surface under constant pressure. After the film was dried, the grating master was carefully removed, leaving a replicated grating structure on the film surface. To further generate a grating pattern, a PDMS mask with the desired pattern was placed on the imprinted film surface. The film was exposed to water vapor once more, selectively removing the grating structure from the unmasked regions. After drying, an RTP-SF film with a well-defined grating pattern was obtained.

Processing of Multidimensional Optical Systems:

1) *System in Figure 4B*: The high-level encrypted QR code system was fabricated by photo-writing a phosphorescent QR code, followed by imprinting a structural color QR code.
2) *System in Figure 4C*: First, a phosphorescent QR code is photo-written on the bottom of the pentahedral precursor. Then, a patterned PMMA nano-coating is applied to the opposite sides of the remaining four faces, after which the precursor is folded into a pentahedral shape.

Amino Acid Analysis: A vial containing 80 mg of SF or RTP-SF films was treated with 20 mL of 6 N HCl, and the films were hydrolyzed at 110 °C for 24 h. An aliquot (≈200 µL) of the hydrolyzed mixture was evaporated to dryness at ≈50 °C for 24 h. The dried residue was reconstituted in 0.02 N HCl to achieve a final concentration of 100 µg mL^{-1}. A 1 mL aliquot of the solution was then injected into a specialized vial for amino acid composition analysis using a Hitachi L-8900 amino acid analyzer.

In Vitro Biodegradation Test: Crystalline SF-Bp-B films (50 mg) were placed in 2 mL centrifuge tubes, and 1.5 mL of protease XIV solution (5 U mL^{-1} in 10 mmol L^{-1} PBS, pH 7.4) was added. The samples were incubated at 37 °C with continuous shaking. At designated time points, the film residues were collected by centrifugation at 10 000 rpm for 5 min, washed three times with deionized water, and dried at 60 °C overnight.

The weight residues of the samples were calculated by the formula:

$$\text{Weight residual rate} = \frac{W_2 - W_0}{W_1 - W_0} \times 100\% \tag{1}$$

where W_0 is the weight of the tube, W_1 is the initial weight of the tube containing films, and W_2 is the weight of the tube containing residual films.

In Vitro Cytotoxicity Test: DMEM medium was supplemented with 10% FBS, 1 ng mL^{-1} basic fibroblast growth factor, 1% non-essential amino acids, and 1% antibiotics/antifungals. This medium was then combined with SF-Bp-B, SF-Nap-B, SF-Py-B, and digest products solutions to achieve final concentrations of 0.25, 0.5, 1, and 1.5 wt.% for each group. Mouse fibroblasts (L-929) were seeded at a density of 1 × 10^4 cells mL^{-1} in 96-well plates and cultured in DMEM medium for 24 h. Afterward, the culture medium was discarded and replaced with a prepared medium containing different concentrations of RTP-SF solutions. After 24 h of incubation, the culture medium was removed, and the cells were incubated in a serum-free medium containing 10% (v/v) AlamarBlue for 2 h. A 100 µL aliquot of the reaction medium was transferred to a black 96-well plate, and fluorescence intensity was measured using a multimode microplate reader (λ_{ex} = 530 nm, λ_{em} = 590 nm, Synergy H1, BioTech). For fluorescence imaging, the cells were washed with PBS and stained with DAPI and TRITC-phalloidin. Fluorescence Images were recorded with a fluorescence microscope (Axio Vert. A1, Carl Zeiss, Germany). The cytoskeleton of cells was shown in red, and the nucleus was shown in blue. The sample size (n) for each experimental group is $n = 5$.

The cell viability of the samples was calculated by the formula:

$$\text{Cell viability} = \frac{A_s - A_b}{A_c - A_b} \times 100\% \tag{2}$$

where A_s is the absorbance value of the sample group, A_b is the absorbance value of the blank group, and A_c is the absorbance value of the control group.

Antibacterial Performance Characterization—Sample Preparation: Briefly, 60 mg of $AgNO_3$ was added to 1 mL of 6% SF solution and mixed thoroughly. After 12 h of illumination with white light, the solution was dialyzed for two days. Then, 1 mL of the dialysate was mixed with 2 mL of an 18% RTP-SF solution. Finally, the antimicrobial nonwoven fabric was obtained by electrostatic spinning at a voltage of 20 kV and an advancement rate of 0.008 mm min^{-1}. To further enhance the antimicrobial properties, the nonwoven fabrics were treated with 75% ethanol for 6 h, followed by immersion in a 20 mg mL^{-1} $AgNO_3$ solution for a set period. Afterward, they were exposed to white light for 12 h to yield the antimicrobial nonwoven fabric.

Antibacterial Performance Characterization—Antibacterial Test: The agar medium, consisting of 2.5 g of Luria-Bertani broth, 1.5 g of agar powder, and 100 mL of distilled water, was autoclaved at 121 °C for 15 min using an autoclave (HVE-50, Hirayama, Japan). After autoclaving, the medium was allowed to cool to ≈40–50 °C. A 15 mL aliquot of the cooled medium was poured into a sterile Petri dish for solidification. A 0.1 mL aliquot of the bacterial suspension (*Escherichia coli* (*E. Coil*) or *Staphylococcus aureus* (*S. Aureus*), at a concentration of 10^6–10^7 CFU mL^{-1}), was evenly spread across the surface of the agar plate and allowed to air-dry. The sample was then placed on the agar plate, and the plate was incubated in an inverted position at 37 °C for 20 h. After incubation, the inhibition zone was observed and recorded. The antibacterial performance was further quantitatively measured according to GB/T 20944.2-2007. The antibacterial rate was calculated according to the formula:

$$\text{Antibacterial rate} = \frac{C_t - T_t}{C_t} \times 100\% \tag{3}$$

where: C_t is the number of colonies cultured on PP nonwoven fabric, and T_t is the number of colonies cultured on PP/RTP-SF nonwoven fabric.

Antibacterial Performance Characterization—Structural and Properties Characterization: UV–vis absorption spectra were collected using a Shimadzu UV-3600. Steady-state photoluminescence/phosphorescence spectra and photoluminescence quantum efficiency were measured using an Edinburgh FLS-980 spectrometer. The fluorescence lifetime and phosphorescence lifetime were measured on FLS-1000. The fluorescence and phosphorescence images were taken by a Canon 850D under the irradiation of a hand-held UV lamp (10 W) of different wavelengths at room temperature. The ^{1}H NMR spectra were recorded on a Bruker Ascend 600 MHz NMR spectrometer using 1 м DMSO-d6/LiCl as the solvent. The ^{13}C NMR spectra were acquired on a Bruker Ascend 400 MHz NMR spectrometer using microsphere powder as the sample. The sample morphologies were characterized using a ULTRA 55 field emission scanning electron microscope with an accelerating voltage of 5 kV and a beam current of 10 µA. Fluorescence images were captured using a fluorescence microscope (Axio Vert. A1, Carl Zeiss, Germany). The spin-coating process was conducted using a spin coater (KW-4A, Chemat, USA) with two stages: an initial spin at 500 rpm for 12 s and a second spin at 3000 rpm for 60 s. The viscosity of RTP-SF solutions and commercial inks (Ink-COM, EPSON T8591) was evaluated using a rheometer (ARES-G2, TA Instruments, USA). Viscosity measurements were performed at 25 °C using a cone-plate geometry (50 mm diameter, 0.0194 rad cone angle). A steady-state flow sweep was conducted over shear rates from 0.1 to 1000 s^{-1}, following a 60 s soak time to equilibrate the sample. The surface tensions of water, commercial ink, and RTP-SF solution were measured using the spinning drop method with an OCA40 contact angle meter at an extrusion rate of 0.1 µL s^{-1}. The structural conformations of the RTP-SF platforms were evaluated using an FTIR spectrometer (INVENIO-S, BRUKER, Germany). All FTIR spectra were collected in the wavenumber range of 4000 to 600 cm^{-1} at 4 cm^{-1} resolution with an average of 64 scans. The filtration performance of the non-woven fabrics (size of 25 × 25 cm) was evaluated using the HR-L8013 testing apparatus. The airflow rate was maintained at 0.35 m s^{-1}, corresponding to a volumetric flow rate of 80 L min^{-1}, following the standard NIOSH 42 CFR 84.

Statistical Analysis: All the data are presented as mean ± standard deviation (SD), and the sample size (n) for each statistical analysis is specified in the respective captions.

Supporting Information

Supporting Information is available from the Wiley Online Library or from the author.

Acknowledgements

This work was supported by the National Key R&D Program of China (No.2021YFA1202000, 2022YFA1203702), the National Natural Science Foundation of China (No. 62175102, T2488302), and the Natural Science Foundation of Jiangsu Province (BK20243067). The authors thank J.-J. He and Prof. S.-C. Tang in the College of Engineering and Applied Sciences, Nanjing University, for assistance in preparing RTP nanofibers.

Conflict of Interest

The authors declare no conflict of interest.

Author Contributions

Y.W. and T.W. conceived the idea and designed the research. T.W. synthesized and characterized phosphorescent silk fibroin. Y.-H.F., J.W., G.L., Z.-C.Z., Z.-T.W., and S.-J.W. assisted in phosphorescence characterizations. J.S. participated in the preparation of phosphorescent microspheres; Q.L. assisted in amino acid analysis. Y.-T.Z. assisted in conducting the in vitro cytotoxicity test. T.W., Z.-Z.Z., and Y.W. contributed to the data analysis. T.W., Y.W., and Y.-Q.L. wrote and revised the manuscript. Y.W. and Y.-Q.L. supervised the research. All authors approved the final version of the manuscript.

Data Availability Statement

The data that support the findings of this study are available from the corresponding author upon reasonable request.

Keywords

biomedical interface, multifunctionality, phosphorescence, silk fibroin, sustainability

Received: July 4, 2025
Revised: September 12, 2025
Published online: September 26, 2025

[1] W. Zhao, Z. He, B. Z. Tang, *Nat. Rev. Mater.* **2020**, *5*, 869.

[2] H. Shi, W. Yao, W. Ye, H. Ma, W. Huang, Z. An, *Acc. Chem. Res.* **2022**, *55*, 3445.

[3] Y. Su, S. Z. F. Phua, Y. Li, X. Zhou, D. Jana, G. Liu, W. Q. Lim, W. K. Ong, C. Yang, Y. Zhao, *Sci. Adv.* **2018**, *4*, aas9732.

[4] J. Wei, C. Liu, J. Duan, A. Shao, J. Li, J. Li, W. Gu, Z. Li, S. Liu, Y. Ma, W. Huang, Q. Zhao, *Nat. Commun.* **2023**, *14*, 627.

[5] L. Gu, H. F. Shi, L. F. Bian, M. X. Gu, K. Ling, X. Wang, H. L. Ma, S. Z. Cai, W. H. Ning, L. S. Fu, H. Wang, S. Wang, Y. R. Gao, W. Yao, F. W. Huo, Y. T. Tao, Z. F. An, X. G. Liu, W. Huang, *Nat. Photon.* **2019**, *13*, 406.

[6] L. Gao, J. Huang, L. Qu, X. Chen, Y. Zhu, C. Li, Q. Tian, Y. Zhao, C. Yang, *Nat. Commun.* **2023**, *14*, 7252.

[7] J. Ma, F. Zeng, X. Lin, Y. Wang, Y. Ma, X. Jia, J. Zhang, B. Liu, Y. Wang, H. Zhao, *Science* **2024**, *385*, 68.

[8] Y. Li, Z. Wu, Z. Huang, C. Yin, H. Tian, X. Ma, *Natl. Sci. Rev.* **2025**, *12*, nwae383.

[9] L. Bian, H. Shi, X. Wang, K. Ling, H. Ma, M. Li, Z. Cheng, C. Ma, S. Cai, Q. Wu, N. Gan, X. Xu, Z. An, W. Huang, *J. Am. Chem. Soc.* **2018**, *140*, 10734.

[10] Y. Zhang, L. Gao, X. Zheng, Z. Wang, C. Yang, H. Tang, L. Qu, Y. Li, Y. Zhao, *Nat. Commun.* **2021**, *12*, 2297.

[11] W. Ye, H. Ma, H. Shi, H. Wang, A. Lv, L. Bian, M. Zhang, C. Ma, K. Ling, M. Gu, Y. Mao, X. Yao, C. Gao, K. Shen, W. Jia, J. Zhi, S. Cai, Z. Song, J. Li, Y. Zhang, S. Lu, K. Liu, C. Dong, Q. Wang, Y. Zhou, W. Yao, Y. Zhang, H. Zhang, Z. Zhang, X. Hang, et al., *Nat. Mater.* **2021**, *20*, 1539.

[12] N. Gan, X. Zou, Z. Qian, A. Lv, L. Wang, H. Ma, H.-J. Qian, L. Gu, Z. An, W. Huang, *Nat. Commun.* **2024**, *15*, 4113.

[13] J. J. Guo, C. L. Yang, Y. L. Zhao, *Acc. Chem. Res.* **2022**, *55*, 1160.

[14] B. Ding, X. Ma, H. Tian, *Acc. Mater. Res.* **2023**, *4*, 827.

[15] X. Yao, H. Ma, X. Wang, H. Wang, Q. Wang, X. Zou, Z. Song, W. Jia, Y. Li, Y. Mao, M. Singh, W. Ye, J. Liang, Y. Zhang, Z. Liu, Y. He, J. Li, Z. Zhou, Z. Zhao, Y. Zhang, G. Niu, C. Yin, S. Zhang, H. Shi, W. Huang, Z. An, *Nat. Commun.* **2022**, *13*, 4890.

[16] D. Li, J. Yang, M. Fang, B. Tang, Z. Li, *Sci. Adv.* **2022**, *8*, abl8392.

[17] Y. Miao, F. Lin, D. Guo, J. Chen, K. Zhang, T. Wu, H. Huang, Z. Chi, Z. Yang, *Sci. Adv.* **2024**, *10*, adk3354.

[18] C. J. Yin, S. Y. Sun, Z. A. Yan, H. L. Hu, P. Jiang, Z. R. Xu, H. Tian, X. Ma, *Proc. Natl. Acad. Sci. USA* **2025**, *122*, 2419481122.

[19] X. Y. Yao, J. Wang, D. J. Jiao, Z. Z. Huang, O. Mhirsi, F. Lossada, L. S. Chen, B. Haehnle, A. J. C. Kuehne, X. Ma, H. Tian, A. Walther, *Adv. Mater.* **2021**, *33*, 2005973.

[20] C. W. Ju, X. C. Wang, B. Li, Q. Ma, Y. Shi, J. Zhang, Y. Xu, Q. Peng, D. Zhao, *Proc. Natl. Acad. Sci. USA* **2023**, *120*, 2310883120.

[21] M. Kukwikila, N. Gale, A. H. El-Sagheer, T. Brown, A. Tavassoli, *Nat. Chem.* **2017**, *9*, 1089.

[22] J. A. Li, L. Zhang, C. Wu, Z. Huang, S. Li, H. Zhang, Q. Yang, Z. Mao, S. Luo, C. Liu, G. Shi, B. Xu, *Angew. Chem., Int. Ed.* **2023**, *62*, 202217284.

[23] J. X. You, C. C. Yin, S. H. Wang, X. Wang, K. F. Jin, Y. R. Wang, J. F. Wang, L. Liu, J. Zhang, J. M. Zhang, *Nat. Commun.* **2024**, *15*, 7149.

[24] J. Liu, Z. P. Song, J. Wei, J. J. Wu, M. Z. Wang, J. G. Li, Y. Ma, B. X. Li, Y. Q. Lu, Q. Zhao, *Adv. Mater.* **2024**, *36*, 2306834.

[25] K. Chen, Y. Zhang, Y. Lei, W. Dai, M. Liu, Z. Cai, H. Wu, X. Huang, X. Ma, *Nat. Commun.* **2024**, *15*, 1269.

[26] K. Wan, B. Tian, Y. Zhai, Y. Liu, H. Wang, S. Liu, S. Li, W. Ye, Z. An, C. Li, J. Li, T. D. James, Z. Chen, *Nat. Commun.* **2022**, *13*, 5508.

[27] X. Zhang, Y. Cheng, J. You, J. Zhang, C. Yin, J. Zhang, *Nat. Commun.* **2022**, *13*, 1117.

[28] Q. Gao, M. Shi, Z. Lü, Q. Zhao, G. Chen, J. Bian, H. Qi, J. Ren, B. Lü, F. Peng, *Adv. Mater.* **2023**, *35*, 2305126.

[29] X. Luo, B. Tian, Y. Zhai, H. Guo, S. Liu, J. Li, S. Li, T. D. James, Z. Chen, *Nat. Rev. Chem.* **2023**, *7*, 800.

[30] Y. Zhai, S. Li, J. Li, S. Liu, T. D. James, J. L. Sessler, Z. Chen, *Nat. Commun.* **2023**, *14*, 2614.

[31] R. Liu, H. Guo, S. Liu, J. Li, S. Li, T. D. James, Z. Chen, *Nat. Commun.* **2024**, *15*, 10588.

[32] A. Reizabal, C. M. Costa, L. Pérez-Álvarez, J. L. Vilas-Vilela, S. Lanceros-Méndez, *Adv. Funct. Mater.* **2022**, *33*, 2210764.

[33] Y. Wang, X. Feng, X. Chen, *Adv. Mater.* **2025**, *37*, 2500073.

[34] C. Li, C. Guo, V. Fitzpatrick, A. Ibrahim, M. J. Zwierstra, P. Hanna, A. Lechtig, A. Nazarian, S. J. Lin, D. L. Kaplan, *Nat. Rev. Mater.* **2019**, *5*, 61.

[35] Z. Zhou, S. Zhang, Y. Cao, B. Marelli, X. Xia, T. H. Tao, *Adv. Mater.* **2018**, *30*, 1706983.

[36] R. Zheng, Y. Wei, Z. C. Zhang, Z. Y. Wang, L. L. Ma, Y. Wang, L. Huang, Y. Q. Lu, *Respons. Mater.* **2023**, *1*, 20230017.

[37] G. Guidetti, L. d'Amone, T. Kim, G. Matzeu, L. Mogas-Soldevila, B. Napier, N. Ostrovsky-Snider, J. Roshko, E. Ruggeri, F. G. Omenetto, *Appl. Phys. Rev.* **2022**, *9*, 011302.

[38] Y. Wang, M. Li, J.-K. Chang, D. Aurelio, W. Li, B. J. Kim, J. H. Kim, M. Liscidini, J. A. Rogers, F. G. Omenetto, *Nat. Commun.* **2021**, *12*, 1651.

[39] H. Liu, Z. Sun, C. Guo, *Adv. Fiber Mater.* **2022**, *4*, 705.

[40] Y. Wang, M. Li, Y. Wang, *Chin. Opt. Lett.* **2020**, *18*, 080004.

[41] G. Guidetti, Y. Wang, F. G. Omenetto, *Nanophotonics* **2020**, *10*, 137.

[42] S. Li, H. Wang, H. Lu, X. Liang, H. Wang, M. Zhang, K. Xia, Z. Yin, Y. Zhang, X. Zhang, Y. Zhang, *Small* **2021**, *17*, 2103623.

[43] L. Xu, X. Liang, S. Zhong, Z. Li, Y. Gao, X. Cui, *ACS Sustain. Chem. Eng.* **2021**, *9*, 12043.

[44] X. Piao, X. Li, G. Wang, T. Wang, K. Zhang, *ACS Mater. Lett.* **2024**, *6*, 2231.

[45] O. Hakimi, D. P. Knight, F. Vollrath, P. Vadgama, *Compos. B. Eng.* **2007**, *38*, 324.

[46] Y. Suzuki, *Polym. J.* **2016**, *48*, 1039.

[47] C. Fu, Z. Shao, V. Fritz, *Chem. Comm.* **2009**, *43*, 6515.

[48] W. Li, Y. Wang, M. Li, L. P. Garbarini, F. G. Omenetto, *Adv. Mater.* **2019**, *31*, 1901036.

[49] Y. E. Ji, Y. Wang, Z. Wang, T. Wang, Y. Fu, Z. Zhu, Y. Wang, L. Ma, Y. Lu, *Laser Photonics Rev.* **2024**, *18*, 2400621.

[50] C. Jiang, T. Wang, Y. Fu, P. Chen, G. Tao, Y. Wang, Y. Lu, *Matter* **2024**, *7*, 1591.

[51] X. Dou, T. Zhu, Z. Wang, W. Sun, Y. Lai, K. Sui, Y. Tan, Y. Zhang, W. Z. Yuan, *Adv. Mater.* **2020**, *32*, 2004768.

[52] H. Peng, G. Xie, Y. Cao, L. Zhang, X. Yan, X. Zhang, S. Miao, Y. Tao, H. Li, C. Zheng, W. Huang, R. Chen, *Sci. Adv.* **2022**, *8*, abk292.

[53] Y. Wang, D. Aurelio, W. Li, P. Tseng, Z. Zheng, M. Li, D. L. Kaplan, M. Liscidini, F. G. Omenetto, *Adv. Mater.* **2017**, *29*, 1702769.

[54] X. Dou, X. Wang, X. Xie, J. Zhang, Y. Li, B. Tang, *Adv. Funct. Mater.* **2024**, *34*, 2314069.

[55] J. H. Kim, S. Jeon, J. H. In, S. Nam, H. M. Jin, K. H. Han, G. G. Yang, H. J. Choi, K. M. Kim, J. Shin, S.-W. Son, S. J. Kwon, B. H. Kim, S. O. Kim, *Nat. Electron.* **2022**, *5*, 433.

[56] Y. H. Chen, C. W. Hwang, S. W. Chang, M. T. Tsai, K. N. Jayakumaran, L. C. Yang, Y. C. Lo, F. H. Ko, H. C. Wang, H. L. Chen, D. Wan, *Adv. Funct. Mater.* **2023**, *33*, 2301924.

[57] O. A. Ogunseitan, J. M. Schoenung, J. D. M. Saphores, A. A. Shapiro, *Science* **2009**, *326*, 670.

[58] C. Ahlneck, G. Zografi, *Int. J. Pharm.* **1990**, *62*, 87.

[59] J. Wang, L. Li, C. Xu, H. Jiang, Q. X. Xie, X. Y. Yang, J. C. Li, H. Xu, Y. Chen, W. Yi, X. J. Hong, Y. Q. Lan, *Adv. Mater.* **2023**, *36*, 2311519.

[60] X. Fei, M. Jia, X. Du, Y. Yang, R. Zhang, Z. Shao, X. Zhao, X. Chen, *Biomacromolecules* **2013**, *14*, 4483.

[61] D. N. Rockwood, R. C. Preda, T. Yücel, X. Wang, M. L. Lovett, D. L. Kaplan, *Nat. Protoc.* **2011**, *6*, 1612.